

# SCIENTIFIC REPORTS



OPEN

## Graphitic Carbon-Coated FeSe<sub>2</sub> Hollow Nanosphere-Decorated Reduced Graphene Oxide Hybrid Nanofibers as an Efficient Anode Material for Sodium Ion Batteries

Jung Sang Cho<sup>1</sup>, Jung-Kul Lee<sup>2</sup> & Yun Chan Kang<sup>1</sup>

Received: 14 January 2016

Accepted: 08 March 2016

Published: 01 April 2016

A novel one-dimensional nanohybrid comprised of conductive graphitic carbon (GC)-coated hollow FeSe<sub>2</sub> nanospheres decorating reduced graphene oxide (rGO) nanofiber (hollow nanosphere FeSe<sub>2</sub>@GC-rGO) was designed as an efficient anode material for sodium ion batteries and synthesized by introducing the nanoscale Kirkendall effect into the electrospinning method. The electrospun nanofibers transformed into hollow nanosphere FeSe<sub>2</sub>@GC-rGO hybrid nanofibers through a Fe@GC-rGO intermediate. The discharge capacities of the bare FeSe<sub>2</sub> nanofibers, nanorod FeSe<sub>2</sub>-rGO-amorphous carbon (AC) hybrid nanofibers, and hollow nanosphere FeSe<sub>2</sub>@GC-rGO hybrid nanofibers at a current density of 1 A g<sup>-1</sup> for the 150th cycle were 63, 302, and 412 mA h g<sup>-1</sup>, respectively, and their corresponding capacity retentions measured from the 2nd cycle were 11, 73, and 82%, respectively. The hollow nanosphere FeSe<sub>2</sub>@GC-rGO hybrid nanofibers delivered a high discharge capacity of 352 mA h g<sup>-1</sup> even at an extremely high current density of 10 A g<sup>-1</sup>. The enhanced electrochemical properties of the hollow nanosphere FeSe<sub>2</sub>@GC-rGO composite nanofibers arose from the synergetic effects of the FeSe<sub>2</sub> hollow morphology and highly conductive rGO matrix.

The demand for large-scale energy storage has increased with the development of electric vehicles (EVs) and renewable energy storage<sup>1-4</sup>. Up to now, lithium ion batteries (LIBs) have been regarded as promising candidates for these applications<sup>5-7</sup>. However, according to the rapidly growing demands for low-cost energy storage, sodium ion batteries (SIBs) may be a feasible alternative because of abundant Na resource (Na is the fourth most abundant element on earth, ~2.6% by weight of the earth's crust) and low cost (cost equivalents in dollars for bulk metal: Na, 0.075; Li, 0.50)<sup>8-10</sup>. However, the larger Na<sup>+</sup> ionic radius (0.76 Å for Li<sup>+</sup> vs 1.02 Å for Na<sup>+</sup>) and molar mass (22.99 g/mol for Li vs 6.94 g/mol for Na) are critical obstacles that affect Na<sup>+</sup> diffusion, resulting in lower specific capacities, lower rate capabilities, larger volume changes, and shorter cycling lives<sup>11-13</sup>.

To overcome these issues, developing efficient anode materials for application in SIBs with good electrochemical performance is urgently needed and desirable. Thus far, one-dimensional (1D) nanomaterials have been recognized as the most desirable materials for applications in energy storage<sup>14-17</sup>. Their unique structures provide enhanced surface-to-volume ratios, short transport lengths for Li<sup>+</sup> ionic transport, and efficient 1D electron transport along their longitudinal directions<sup>14-17</sup>. Hollow structures also have exhibited good electrochemical properties at high current densities because of their decreased ion diffusion lengths and the increased contact areas between the electrolyte and electrode for Li<sup>+</sup> insertion-desertion<sup>18-22</sup>. Moreover, the void spaces in such structures could accommodate the volume change during cycling<sup>23-25</sup>. However, larger Na<sup>+</sup> ionic radius compared to that of Li<sup>+</sup> seems to prevent the achievement of sufficiently good electrochemical properties of anode materials in SIBs even when the advantageous effects of the 1D nanomaterials and the hollow structure are combined. To surmount this, construction of a stable artificial coating layer on the surface of the hollow structure

<sup>1</sup>Department of Materials Science and Engineering, Korea University, Anam-Dong, Seongbuk-Gu, Seoul 136-713, Republic of Korea. <sup>2</sup>Department of Chemical Engineering, Konkuk University, 1 Hwayang-dong, Gwangjin-gu, Seoul 143-701, Republic of Korea. Correspondence and requests for materials should be addressed to J.-K.L. (email: jkrhee@konkuk.ac.kr) or Y.C.K. (email: yckang@korea.ac.kr)

would be another effective strategy for further maintaining the structural integrity via accommodating the huge volume variations induced by  $\text{Na}^+$  diffusion<sup>26</sup>. Herein, the conductive graphitic carbon (GC) could be applied as a suitable coating layer that plays the role mentioned above and it could derivatively serve as fast and continuous transport pathways for electrons upon cycling due to its high electroconductivity. Additionally, the stable GC coating layer on the hollow structure triggers stable solid electrolyte interphase (SEI) formation which is usually formed in cycling owing to the reductive decomposition of organic electrolytes. Along with these structural strategies, graphene is considered as the most promising matrix to support anode materials in SIBs due to its prominent advantages, such as its superior electrical conductivity, high specific surface area, structural flexibility, and chemical stability, all of which are responsible for improved electrochemical performance in SIBs<sup>27–30</sup>. In this context, hybrid nanomaterials consisting of highly conductive graphene and the hollow structure with GC coating layer is expected to be a tactic for efficient anode materials in SIBs with good electrochemical performance.

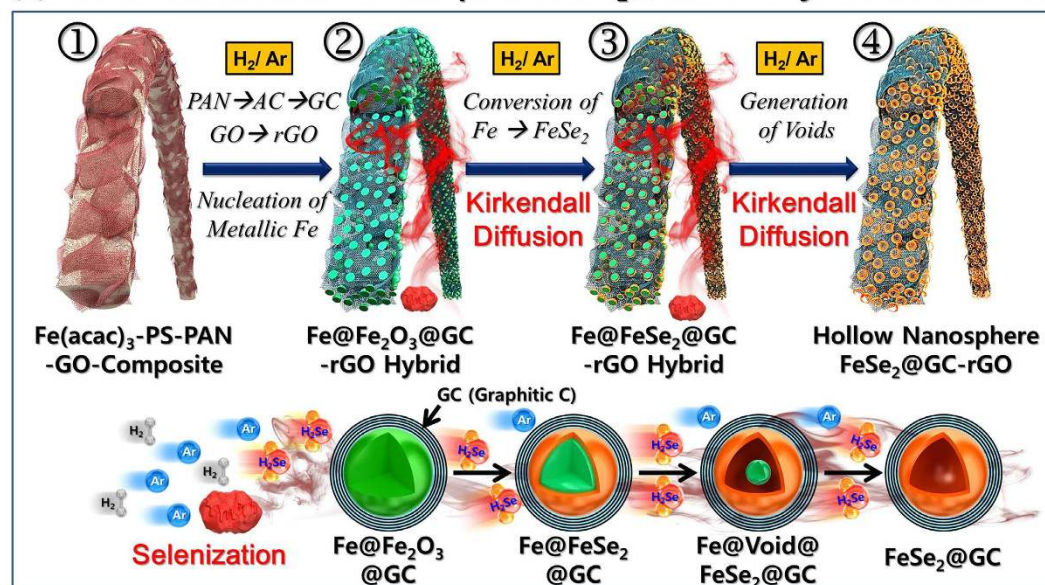
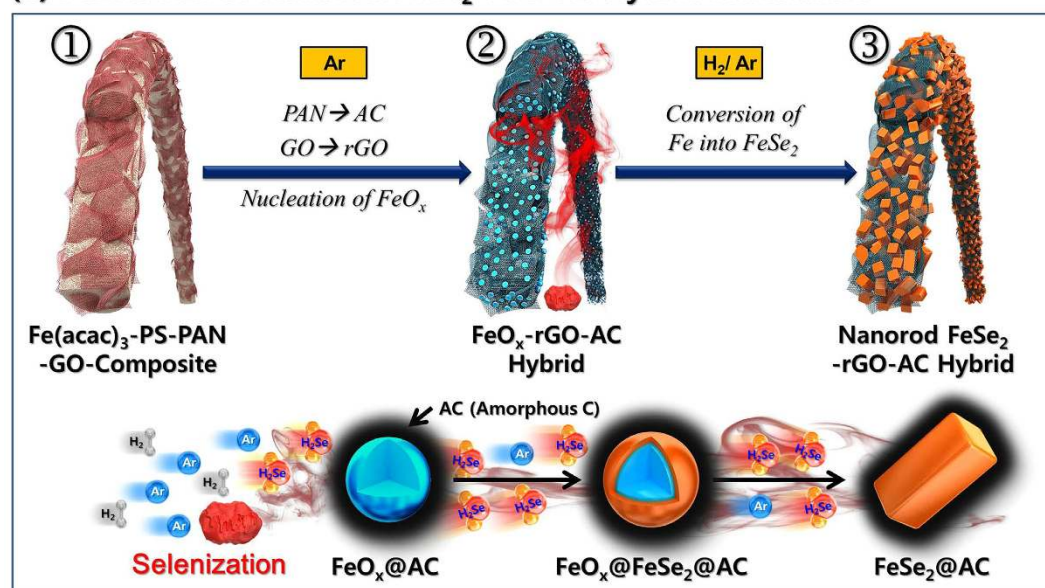
Herein, we designed 1D nanomaterials comprising graphitic carbon (GC)-coated hollow metal chalcogenide nanospheres decorated within a reduced graphene oxide (rGO) nanofiber (hollow nanosphere  $\text{FeSe}_2$ @GC-rGO). Novel-structured rGO nanofibers comprising graphitic carbon-coated  $\text{FeSe}_2$  hollow nanospheres selected as the first target material were prepared by applying the nanoscale Kirkendall diffusion process to the conventional electrospinning process in order to create this anode material for SIBs, although there has been scarce study concerning the electrochemical-reaction mechanism of  $\text{FeSe}_2$  for SIBs. The electrochemical properties of the  $\text{FeSe}_2$ @GC-rGO hybrid nanofibers comprising  $\text{FeSe}_2$  hollow nanospheres were compared with those of the bare  $\text{FeSe}_2$  nanofibers and  $\text{FeSe}_2$ -rGO-amorphous carbon (AC) hybrid nanofibers comprising  $\text{FeSe}_2$  nanorods.

## Results and Discussion

The formation mechanism of the hollow nanosphere  $\text{FeSe}_2$ @GC-rGO hybrid nanofibers is described in Fig. 1a. The composite nanofibers composed of PAN, PS, GO, and  $\text{Fe}(\text{acac})_3$  were prepared via an electrospinning process (Fig. 1a-①). A reduction process of these electrospun nanofibers under a  $\text{H}_2/\text{Ar}$  atmosphere at 500 °C produced the metallic  $\text{Fe}$ @GC-rGO hybrid nanofibers (Fig. 1a-②). Reduction of the GO nanosheets into rGO and carbonization of PAN into amorphous carbon (AC) material occurred during this reduction process. The AC covering the Fe nanocrystals changed into graphitic carbon (GC) during reduction, a process for which the metallic Fe nanocrystals acted as a catalyst. Decomposition of PS into gases even under the  $\text{H}_2/\text{Ar}$  atmosphere resulted in metallic Fe-rGO-GC hybrid nanofibers with a minimum content of amorphous carbon with low electrical conductivity and a high initial irreversible-capacity loss. The metallic Fe-rGO-GC hybrid nanofibers transformed into hollow nanosphere  $\text{FeSe}_2$ @GC-rGO hybrid nanofibers via a selenization process under  $\text{H}_2\text{Se}$  gas, which was formed from Se powders via a reaction with  $\text{H}_2$  gas (Fig. 1a-③). The Fe nanocrystals with solid structures comprising the hybrid nanofibers transformed into the  $\text{FeSe}_2$  hollow nanospheres via the well-known nanoscale Kirkendall diffusion process [Fe cations diffused outward more quickly than Se anion diffused inward, which is consistent with the larger ionic radius of Se anions ( $\text{Se}^{2-}$  is 184 pm) than Fe cations ( $\text{Fe}^{2+}$  is 76 pm,  $\text{Fe}^{3+}$  is 65 pm,  $\text{Fe}^{4+}$  is 72 pm)] through intermediate yolk-shell-structured nanopowders with the configuration  $\text{Fe@void@FeSe}_2$  (Fig. 1a-③,④). The formation mechanism of the nanorod  $\text{FeSe}_2$ -rGO-AC hybrid nanofiber is shown in Fig. 1b. The carbonization process of the composite nanofibers composed of PAN, PS, GO, and  $\text{Fe}(\text{acac})_3$  under Ar atmosphere at 500 °C produced the  $\text{FeO}_x$ -rGO-AC hybrid nanofibers (Fig. 1b-①,②). The selenization of  $\text{FeO}_x$  nanocrystals formed the  $\text{FeSe}_2$  nanorods surrounded by amorphous carbon (AC) (Fig. 1b-③). In this case, graphitization of the amorphous carbon did not occur due to the absence of a metallic Fe catalyst.

The morphologies of the electrospun nanofibers are shown in Fig. S1a. The composite nanofibers composed of PAN, PS, GO, and  $\text{Fe}(\text{acac})_3$  with a mean diameter of 3  $\mu\text{m}$  had filled structures and smooth surfaces. The morphologies of the metallic  $\text{Fe}$ @GC-rGO hybrid nanofibers obtained after the reduction process are shown in Fig. 2. The electrospun nanofibers transformed into nanofibers with porous and withered structures via the reduction process. The TEM images shown in Fig. 2b,c reveal the ultrafine nanopowders uniformly dispersed within the hybrid nanofibers. The nanopowders shown in Fig. 2d had yolk-shell structures with the configuration  $\text{Fe@void@Fe}_2\text{O}_3$ . The exposure of ultrafine Fe nanocrystals under an air atmosphere at room temperature after the reduction process formed the  $\text{Fe}_2\text{O}_3$  layer via surface oxidation. The diffusion out of the Fe component into the surface of the nanopowders via nanoscale Kirkendall diffusion formed the nanopowders with the yolk-shell structures. The nanopowder shown in the high-resolution TEM image in Fig. 2e had a double-shelled structure with the configuration  $\text{Fe@Fe}_2\text{O}_3$ @GC (graphitic carbon). The graphitic carbon formed due to the Fe catalyst uniformly covering the  $\text{Fe@Fe}_2\text{O}_3$  nanopowder. The high-resolution TEM image shown in Fig. 2e revealed clear lattice fringes separated by 0.203, 0.252, 0.340 nm, which correspond to the (110), (110), and (001) crystal planes of Fe,  $\text{Fe}_2\text{O}_3$ , and graphitic carbon phase, respectively. The SAED and XRD patterns shown in Figs 2f and S2, respectively, revealed the formation of the  $\text{Fe}$ @GC-rGO hybrid nanofibers. The SAED pattern revealed the presence of (110), (200), and (211) lattice planes corresponding to the Fe phase, as well as (113) plane of  $\text{Fe}_2\text{O}_3$  phase due to the partial surface oxidation of Fe nanocrystals by exposure in air. The elemental-mapping images shown in Fig. 2g revealed the uniform distribution of the Fe nanocrystals over the hybrid nanofibers. The trace amounts of oxygen due to surface oxidation of the Fe nanocrystals was observed from the elemental-mapping image.

The morphologies of the hollow nanosphere  $\text{FeSe}_2$ @GC-rGO hybrid nanofibers formed via the selenization process of the metallic  $\text{Fe}$ @GC-rGO hybrid nanofibers are shown in Fig. 3. The overall morphology of these nanofibers did not change during the selenization process. However, the inner structure of the nanofibers observable in the TEM images strictly changed with the selenization process. The hybrid nanofibers were composed with hollow nanospheres formed via the nanoscale Kirkendall diffusion process. The high-resolution TEM image shown in Fig. 3e revealed clear lattice fringes separated by 0.256 and 0.340 nm, which corresponded to the (111) and (001) crystal planes of  $\text{FeSe}_2$  and graphitic carbon, respectively. The SAED and XRD patterns shown in Figs 3f and S2, respectively, revealed the formation of the  $\text{FeSe}_2$ @GC-rGO hybrid nanofibers. The Fe-to-Se component ratio observed from the energy dispersive spectroscopy (EDS) analysis shown in Fig. S3 was approximately 2.

**(a) Formation of Hollow Nanosphere FeSe<sub>2</sub>@GC-rGO Hybrid Nanofibers****(b) Formation of Nanorod FeSe<sub>2</sub>-rGO-AC Hybrid Nanofibers**

**Figure 1.** Schematic diagram for the formation mechanism of (a) hollow nanosphere FeSe<sub>2</sub>@GC-rGO and (b) nanorod FeSe<sub>2</sub>-decorated rGO-AC hybrid nanofibers.

The Raman spectrum shown in Fig. S4 contained the characteristic wide *D* and *G* bands of carbon around 1340 and 1590 cm<sup>-1</sup>, respectively. The higher signal peak intensity of the *D* band compared to that of the *G* band is indicative of the thermal reduction of GO nanosheets to rGO nanosheets during the post-heat-treatment process<sup>31</sup>. The elemental-mapping images shown in Fig. 3g revealed the uniform distribution of the FeSe<sub>2</sub> hollow nanospheres over the hybrid nanofibers.

The chemical state and molecular environment of the metallic Fe@GC-rGO and hollow nanosphere FeSe<sub>2</sub>@GC-rGO hybrid nanofibers were characterized via X-ray photoelectron spectroscopy (XPS). In the Fe 2*p* spectrum of the metallic Fe@GC-rGO hybrid nanofibers shown in Fig. S5a, there were two peaks at binding energies of 711 eV for Fe 2*p*<sub>3/2</sub> and 724 eV for Fe 2*p*<sub>1/2</sub>, which are the characteristic peaks of Fe(III) in *a*-Fe<sub>2</sub>O<sub>3</sub> due to the partial surface oxidation of the Fe nanocrystals by exposure in air<sup>14</sup>. In the Fe 2*p* spectrum of the hollow nanosphere FeSe<sub>2</sub>@GC-rGO hybrid nanofibers shown in Fig. S5b, the main peaks observed occurred at binding energies of 706 eV for Fe 2*p*<sub>3/2</sub> and 720 eV for Fe 2*p*<sub>1/2</sub>; these are characteristic of FeSe<sub>2</sub> and a shake-up satellite<sup>32</sup>. In the Se 3*d* spectrum in Fig. S5c, the binding energies at 54.55 eV for Se 3*d*<sub>5/2</sub> and 55.31 eV for Se 3*d*<sub>3/2</sub> were also confirmed to be in good agreement with the reported values for FeSe<sub>2</sub> in the literature<sup>32</sup>. Additionally, the Se–O bond observed at 58.2 eV revealed the existence of a small amount of SeO<sub>2</sub> impurities formed during the

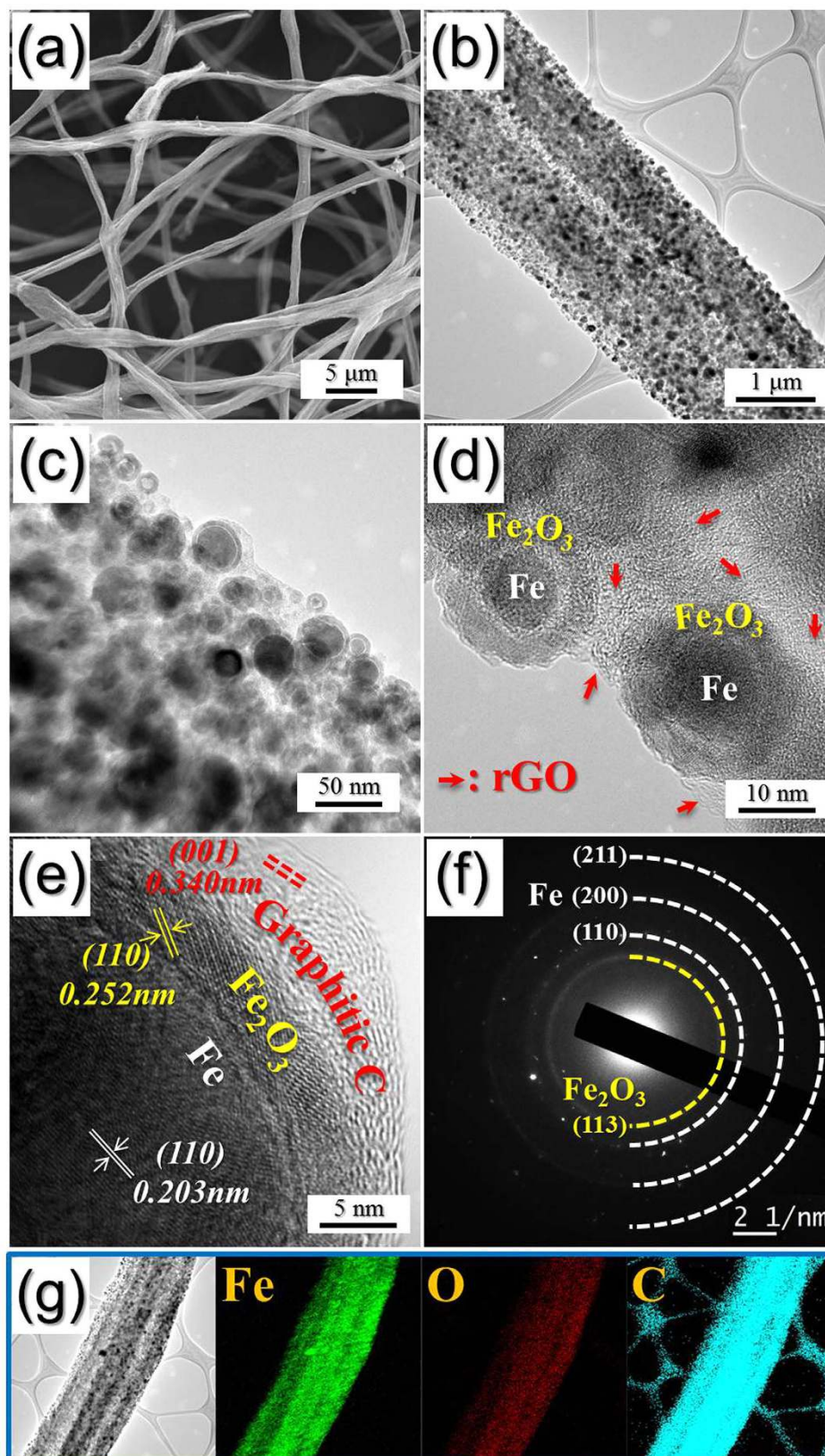


**Figure 2.** Morphologies, SAED pattern, and elemental mapping images of the Fe@GC-rGO hybrid nanofibers: (a) SEM image, (b–d) TEM images, (e) HR-TEM image, (f) SAED pattern, and (g) elemental mapping images.

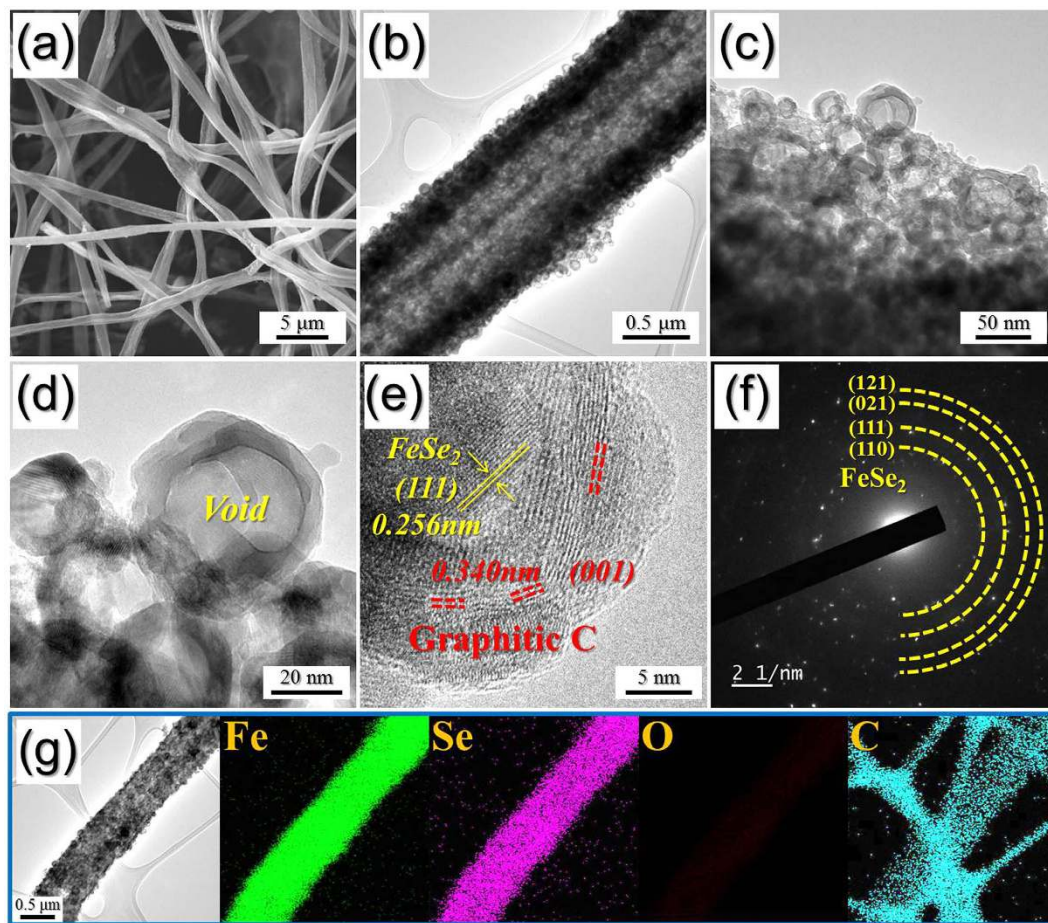


**Figure 3.** Morphologies, SAED pattern, and elemental mapping images of the hollow nanosphere  $\text{FeSe}_2$ @GC-rGO hybrid nanofibers: (a) SEM image, (b–d) TEM images, (e) HR-TEM image, (f) SAED pattern, and (g) elemental mapping images.

selenization process. The C 1s peak shown in Fig. S5d revealed peaks corresponding to  $sp^2$ -bonded carbon (C–C), epoxy and alkoxy groups (C–O), and carbonyl and carboxylic (C=O) components at 284.6, 286.6, and 288.1 eV, respectively<sup>10</sup>. The C–C bond peak was strong, while the C–O and C=O peaks were weak, indicating the thermal reduction of the GO nanosheets to rGO nanosheets during the two-step post-treatment preparation process. The TG curve of the hollow nanosphere  $\text{FeSe}_2$ @GC-rGO hybrid nanofibers shown in Fig. S6 revealed a one-step weight increase and two-step weight loss for temperatures below 600 °C. The partial oxidation reaction of  $\text{FeSe}_2$  with oxygen resulted in a weight increase around 230 °C. The two-step weight loss observed at temperatures between 250 and 500 °C was attributed to the decomposition of  $\text{FeSe}_2$  into  $\text{Fe}_2\text{O}_3$  and the combustion of rGO and GC. The rGO-GC content of 27% was estimated from the TG analysis of the hollow nanosphere  $\text{FeSe}_2$ @GC-rGO hybrid nanofibers.

Bare  $\text{FeSe}_2$  and nanorod  $\text{FeSe}_2$ -rGO-AC hybrid nanofibers as the comparison samples were also prepared via a selenization process of the bare  $\text{Fe}_2\text{O}_3$  and  $\text{FeO}_x$ -rGO-AC hybrid nanofibers, respectively. The bare  $\text{Fe}_2\text{O}_3$  nanofibers shown in Fig. S7 were formed via the oxidation of the electrospun nanofibers under an air atmosphere at 500 °C. The bare  $\text{Fe}_2\text{O}_3$  nanofibers with cubic structure transformed into bare  $\text{FeSe}_2$  nanofibers with orthorhombic structure via the selenization process shown in Figs S7 and S8. The ultrafine  $\text{Fe}_2\text{O}_3$  nanocrystals transformed into the submicron-sized  $\text{FeSe}_2$  crystals during the selenization process. The high-resolution TEM image shown in Fig. S8d revealed clear lattice fringes separated by 0.287 nm, which corresponded to the (110) crystal plane of  $\text{FeSe}_2$  phase. The SAED and XRD patterns shown in Fig. S8e,f, respectively, revealed the formation of the phase pure  $\text{FeSe}_2$  nanofibers. In addition, the elemental-mapping images shown in Fig. S8g revealed the formation of carbon-free  $\text{FeSe}_2$  nanofibers.

The nanorod  $\text{FeSe}_2$ -rGO-AC hybrid nanofibers prepared via the selenization of the  $\text{FeO}_x$ -rGO-AC hybrid nanofibers also had a unique structure. The  $\text{FeSe}_2$  nanorods were uniformly embedded within the rGO-AC nanofibers, as shown by the SEM and TEM images in Fig. 4a–c. The mean thickness of the  $\text{FeSe}_2$  nanorods measured from the TEM images was 148 nm. The high-resolution TEM image shown in Fig. 4d revealed clear lattice fringes separated by 0.256 nm, which corresponded to the (111) crystal plane of  $\text{FeSe}_2$  phase. The SAED and XRD patterns shown in Fig. 4e,f, respectively, revealed the formation of the  $\text{FeSe}_2$ -rGO-AC hybrid nanofibers with a pure crystal structure of the  $\text{FeSe}_2$  phase. The elemental-mapping images shown in Fig. 4g revealed a uniform distribution of  $\text{FeSe}_2$  nanocrystals within the rGO-AC hybrid matrix. The  $\text{N}_2$ -adsorption and -desorption isotherms

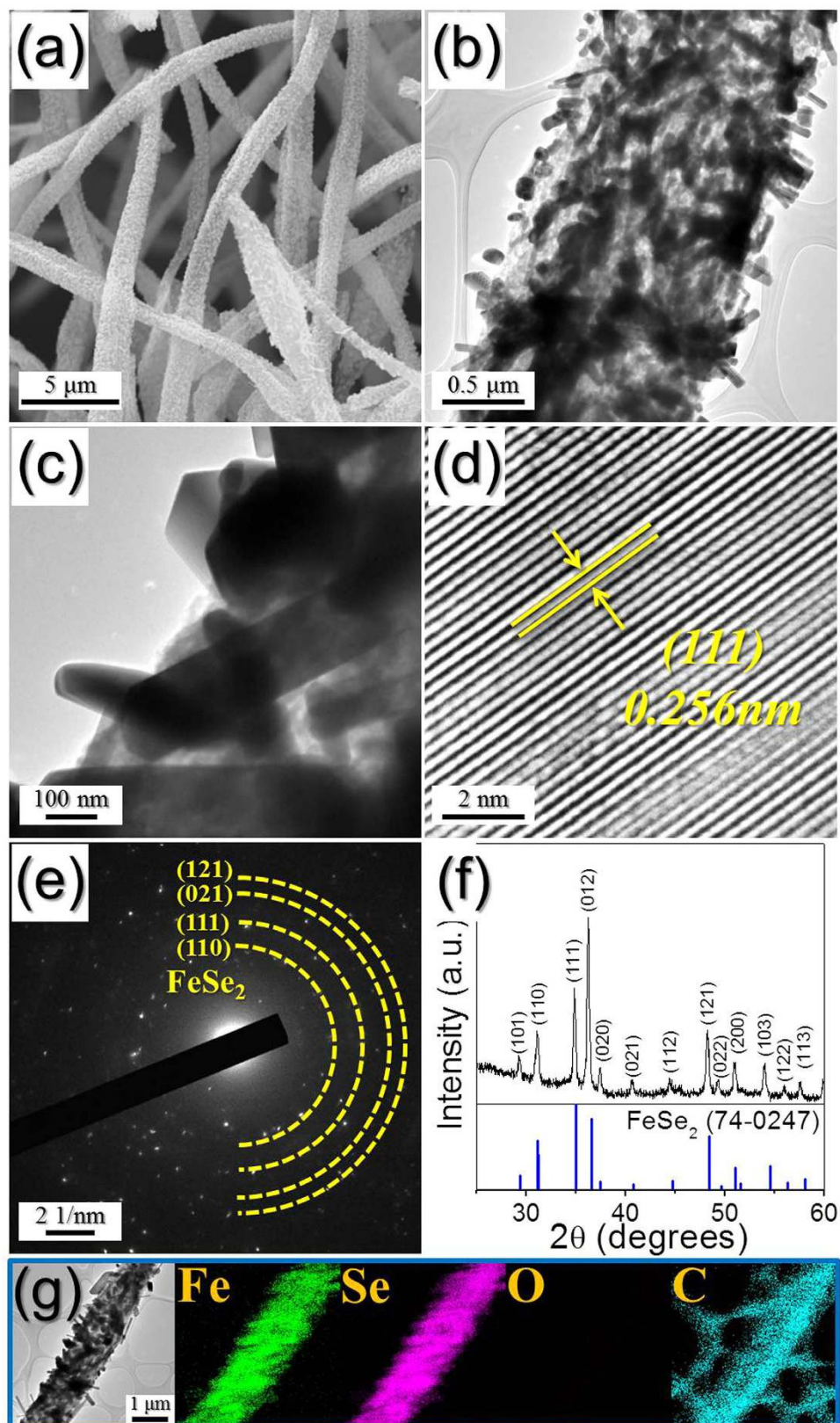


**Figure 4.** Morphologies, SAED pattern, XRD pattern, and elemental mapping images of the nanorod  $\text{FeSe}_2$ -rGO-AC hybrid nanofibers: (a) SEM, (b,c) TEM images, (d) HR-TEM image, (e) SAED pattern, (f) XRD pattern, and (g) elemental mapping images.

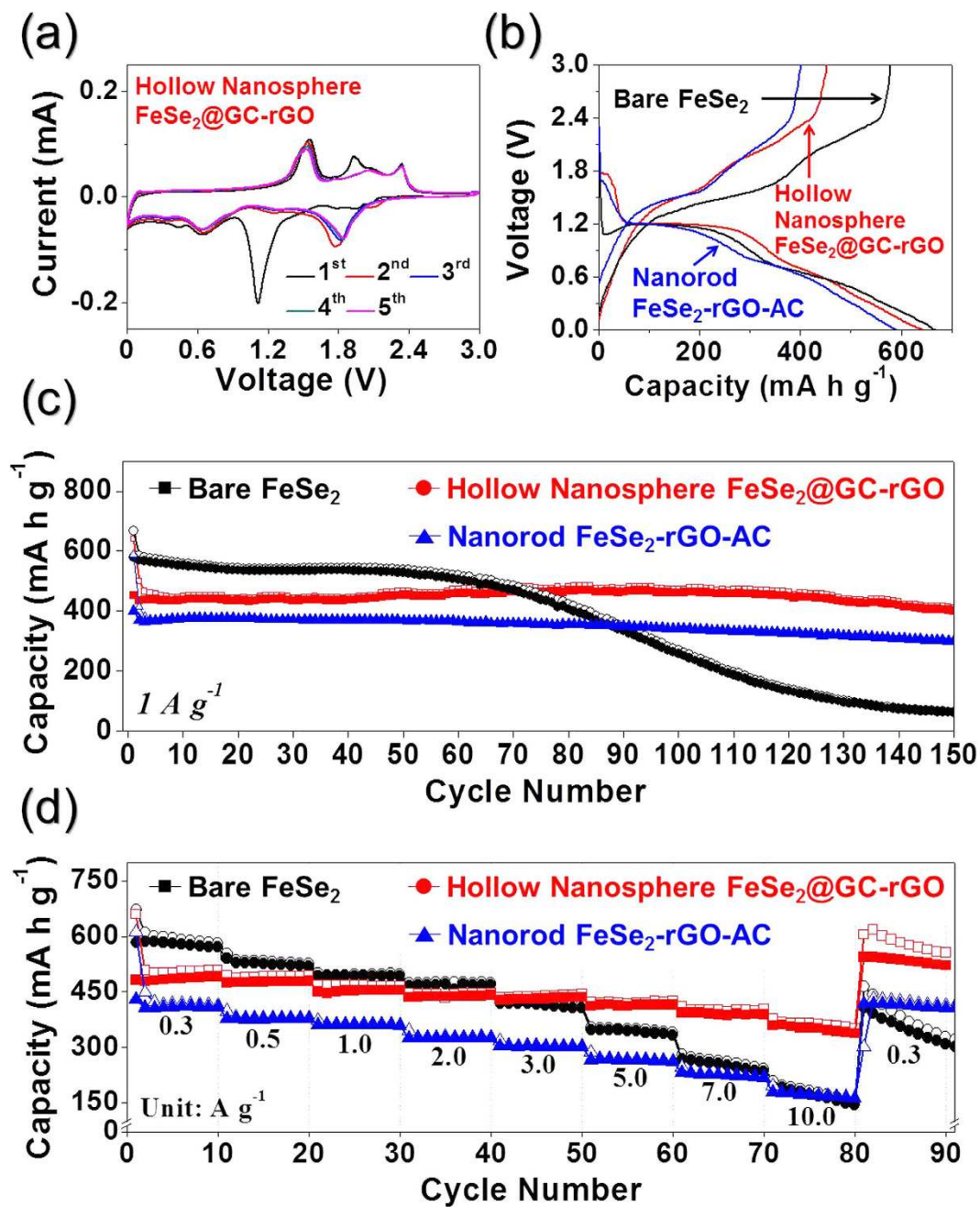


**Figure 5.** Electrochemical properties of the hollow FeSe<sub>2</sub>@GC-rGO hybrid, nanorod FeSe<sub>2</sub>-rGO-AC hybrid, and bare FeSe<sub>2</sub> nanofibers: (a) CV curves of the hollow FeSe<sub>2</sub>@GC-rGO hybrid nanofibers, (b) first charge-discharge curves at a current density of 1.0 A g<sup>-1</sup>, (c) cycling performances at a current density of 1.0 A g<sup>-1</sup>, and (d) rate performances.

and BJH pore size distributions of the three samples are shown in Fig. S9. The BET surface areas of the bare FeSe<sub>2</sub>, nanorod FeSe<sub>2</sub>-rGO-AC, and hollow nanosphere FeSe<sub>2</sub>@GC-rGO hybrid nanofibers were 4, 9, and 34 m<sup>2</sup> g<sup>-1</sup>, respectively. The nanorod FeSe<sub>2</sub>-rGO-AC and hollow nanosphere FeSe<sub>2</sub>@GC-rGO hybrid nanofibers showed well-developed mesopores due to their carbon materials.

The electrochemical properties of the hollow nanosphere FeSe<sub>2</sub>@GC-rGO hybrid nanofibers for sodium ion storage were compared with those of the bare FeSe<sub>2</sub> and nanorod FeSe<sub>2</sub>-rGO-AC hybrid nanofibers via cyclic voltammograms (CVs) and galvanostatic discharge-charge cycling in a voltage range of 0.001–3.0 V vs Na/Na<sup>+</sup>. The CVs of the hollow nanosphere FeSe<sub>2</sub>@GC-rGO hybrid nanofibers during the first five cycles at a scan rate of 0.07 mV s<sup>-1</sup> are shown in Fig. 5a. The first cathodic scan of the hollow nanosphere FeSe<sub>2</sub>@GC-rGO hybrid nanofibers showed three distinct peaks located at 1.1, 0.7, and 0.4 V. The sharp reduction peak located at 1.1 V was attributed to the formation of Na<sub>x</sub>FeSe<sub>2</sub><sup>33</sup> and the formation of a solid electrolyte interphase (SEI) by electrolyte decomposition<sup>34</sup>. The two reduction peaks located at 0.7 and 0.4 V were attributed to the formations of FeSe

and  $\text{Na}_2\text{Se}$ , first, and Fe and  $\text{Na}_2\text{Se}$ , second, respectively<sup>33</sup>. During the anodic scans, three oxidation peaks were observed at 1.6, 1.9 and 2.3 V, which were attributed to the formation of  $\text{Na}_x\text{FeSe}_2$  and  $\text{FeSe}_2$ , and the subsequent decomposition of the SEI layer, respectively<sup>33–36</sup>. The cathodic scans from the second cycle onward showed distinct reduction peaks at around 1.8 V. The formation of ultrafine  $\text{FeSe}_2$  nanocrystals during the first discharge and charge processes resulted in the reduction peak shift to a high potential. The CV curves of the bare  $\text{FeSe}_2$  and nanorod  $\text{FeSe}_2$ -rGO-AC hybrid nanofibers shown in Fig. S10 had similar shapes to those of the hollow nanosphere  $\text{FeSe}_2$ @GC-rGO hybrid nanofibers. The initial discharge and charge curves of the three samples at a current density of  $1 \text{ A g}^{-1}$  are shown in Fig. 5b. The initial discharge capacities of the bare  $\text{FeSe}_2$ , nanorod  $\text{FeSe}_2$ -rGO-AC, and hollow nanosphere  $\text{FeSe}_2$ @GC-rGO hybrid nanofibers were 667, 589, and  $642 \text{ mA h g}^{-1}$ , respectively, and their corresponding initial charge capacities were 578, 401, and  $452 \text{ mA h g}^{-1}$ , respectively. The nanorod  $\text{FeSe}_2$ -rGO-AC and hollow nanosphere  $\text{FeSe}_2$ @GC-rGO hybrid nanofibers had lower initial Coulombic efficiencies than that of the bare  $\text{FeSe}_2$  nanofibers due to the high initial irreversible-capacity loss of the carbon material. The cycling performances of the three samples at a current density of  $1 \text{ A g}^{-1}$  are shown in Fig. 5c. The nanorod  $\text{FeSe}_2$ -rGO-AC and hollow nanosphere  $\text{FeSe}_2$ @GC-rGO hybrid nanofibers had superior cycling performances compared to that of the bare  $\text{FeSe}_2$  nanofibers. The discharge capacities of the bare  $\text{FeSe}_2$ , nanorod  $\text{FeSe}_2$ -rGO-AC, and hollow nanosphere  $\text{FeSe}_2$ @GC-rGO hybrid nanofibers for the 150<sup>th</sup> cycle were 63, 302, and  $412 \text{ mA h g}^{-1}$ , and their corresponding capacity retentions measured from the 2<sup>nd</sup> cycle were 11, 73, and 82%, respectively. The initial discharge and charge curves of the nanorod  $\text{FeSe}_2$ -rGO-AC and hollow nanosphere  $\text{FeSe}_2$ @GC-rGO hybrid nanofibers at a low current density of  $0.05 \text{ A g}^{-1}$  are shown in Fig. S11, in which the two samples had similar initial discharge and charge capacities. Therefore, in Fig. 5c, the fast sodium ion insertion and desorption in the hollow nanosphere  $\text{FeSe}_2$ @GC-rGO hybrid nanofibers with their unique structure resulted in higher capacities than those of the nanorod  $\text{FeSe}_2$ -rGO-AC hybrid nanofibers at a high current density of  $1 \text{ A g}^{-1}$ . The rate performances of the three samples are shown in Fig. 5d in which the current density was increased stepwise from 0.3 to  $10 \text{ A g}^{-1}$ . The hollow nanosphere  $\text{FeSe}_2$ @GC-rGO hybrid nanofibers showed superior rate performance compared to those of the bare  $\text{FeSe}_2$  and nanorod  $\text{FeSe}_2$ -rGO-AC hybrid nanofibers. The gap between the discharge capacities of the nanorod  $\text{FeSe}_2$ -rGO-AC and hollow nanosphere  $\text{FeSe}_2$ @GC-rGO hybrid nanofibers showing good cycling performances for sodium ion storage increased with increasing current densities. The hollow nanosphere  $\text{FeSe}_2$ @GC-rGO hybrid nanofibers had final discharge capacities of 510, 494, 466, 448, 443, 425, 404 and  $352 \text{ mA h g}^{-1}$  at current densities of 0.3, 0.5, 1.0, 2.0, 3.0, 5.0, 7.0, and  $10 \text{ A g}^{-1}$ , respectively. The discharge capacities of the hollow nanosphere  $\text{FeSe}_2$ @GC-rGO hybrid nanofibers were well recovered to  $605 \text{ mA h g}^{-1}$  when the current density was returned to  $0.3 \text{ A g}^{-1}$  after cycling at high current densities. The formation of a polymeric gel-like film on the active material resulted in the high capacities of the hollow nanosphere  $\text{FeSe}_2$ @GC-rGO hybrid when the current density was returned to  $0.3 \text{ A g}^{-1}$  after cycling at high current densities.

Electrochemical-impedance-spectroscopy (EIS) measurements of the three samples were taken before and after 1, 20, 50, and 70 cycles to investigate the superior sodium ion storage properties of the hollow nanosphere  $\text{FeSe}_2$ @GC-rGO hybrid nanofibers compared to those of bare  $\text{FeSe}_2$  and nanorod  $\text{FeSe}_2$ -rGO-AC hybrid nanofibers. The Nyquist plots shown in Fig. 6 were deconvoluted with a Randle-type equivalent circuit model (Fig. S12). The equivalent circuit model describes the electrochemical reaction steps, including Na ion migration through SEI layers, a charge transfer reaction, and Na ion diffusion kinetics throughout the active materials. The nanorod  $\text{FeSe}_2$ -rGO-AC hybrid nanofibers with high conductivity originated by AC, and lower surface area compared to hollow nanosphere  $\text{FeSe}_2$ @GC-rGO had lower  $R_{ct}$  than those of the other two nanofibers before cycling, as shown in Fig. 6a. The  $R_{ct}$  values of the three samples decreased abruptly after the first cycle due to the transformation of the  $\text{FeSe}_2$  crystals into ultrafine nanocrystals during the first cycle<sup>37–39</sup>. The  $R_{ct}$  values of the bare  $\text{FeSe}_2$  nanofibers increased strictly during cycling, as shown in Fig. 6b. However, the  $R_{ct}$  values of the hollow nanosphere  $\text{FeSe}_2$ @GC-rGO and nanorod  $\text{FeSe}_2$ -rGO-AC hybrid nanofibers remained constant during 70 cycles, as shown in Fig. 6c,d, respectively. The  $R_{ct}$  values of the bare  $\text{FeSe}_2$ , nanorod  $\text{FeSe}_2$ -rGO-AC, and hollow nanosphere  $\text{FeSe}_2$ @GC-rGO hybrid nanofibers after 70 cycles were 79, 41, and  $41 \Omega$ , respectively. The results of the EIS measurements revealed the structural stability of the hollow nanosphere  $\text{FeSe}_2$ @GC-rGO and nanorod  $\text{FeSe}_2$ -rGO-AC hybrid nanofibers during the repeated Na insertion and extraction processes. In contrast, the structural destruction during cycling increased the  $R_{ct}$  values of the bare  $\text{FeSe}_2$  nanofibers. Therefore, the structural stability and fast sodium insertion and desorption characteristics of the hollow nanosphere  $\text{FeSe}_2$ @GC-rGO hybrid nanofibers correlated to their excellent Na ion storage properties.

The morphologies of the hollow nanosphere  $\text{FeSe}_2$ @GC-rGO hybrid, nanorod  $\text{FeSe}_2$ -rGO-AC hybrid, and bare  $\text{FeSe}_2$  nanofibers obtained after the 100<sup>th</sup> cycle, are shown in Fig. 7. The hollow nanosphere  $\text{FeSe}_2$ @GC-rGO hybrid nanofibers maintained their original morphologies well even after long-term cycling as shown by TEM images in Fig. 7a, in which the hollow structure of the  $\text{FeSe}_2$  nanospheres was well observed. The nanorod  $\text{FeSe}_2$ -rGO-AC hybrid nanofibers had also maintained overall morphologies after cycling, as shown in Fig. 7b. However, the structure of the bare  $\text{FeSe}_2$  nanofibers completely destroyed after cycling, as shown in Fig. 7c.

These enhanced electrochemical properties of the hollow nanosphere  $\text{FeSe}_2$ @GC-rGO hybrid nanofibers arose from the synergetic effects of the highly conductive rGO nano-network matrix composing the fiber and the  $\text{FeSe}_2$  hollow sphere encapsulated within GC coating layer. First of all, rGO nano-network matrix surrounding the  $\text{FeSe}_2$ @GC spheres acted as efficient conductive channels for electrons to transfer easily, as shown in Fig. 8a. Along with this, rGO nano-network matrix could act as a buffer to accommodate the volume variation of  $\text{FeSe}_2$ @GC spheres during repeated cycling by wrapping the spheres. In addition to the role of rGO nano-network matrix,  $\text{FeSe}_2$  hollow sphere with GC coating layer played at least three significant roles for further improvement in the electrochemical properties. First,  $\text{FeSe}_2$  hollow sphere lowered  $\text{Na}^+$  diffusion-induced stresses, consequently alleviating the volume variations upon  $\text{Na}^+$  insertion and desorption, and also had short diffusion length for  $\text{Na}^+$ , increased contact area between the electrolyte and electrode in comparison with solid structures. Second, the highly conductive GC coating layer on the  $\text{FeSe}_2$  hollow sphere could primarily serve as fast and continuous



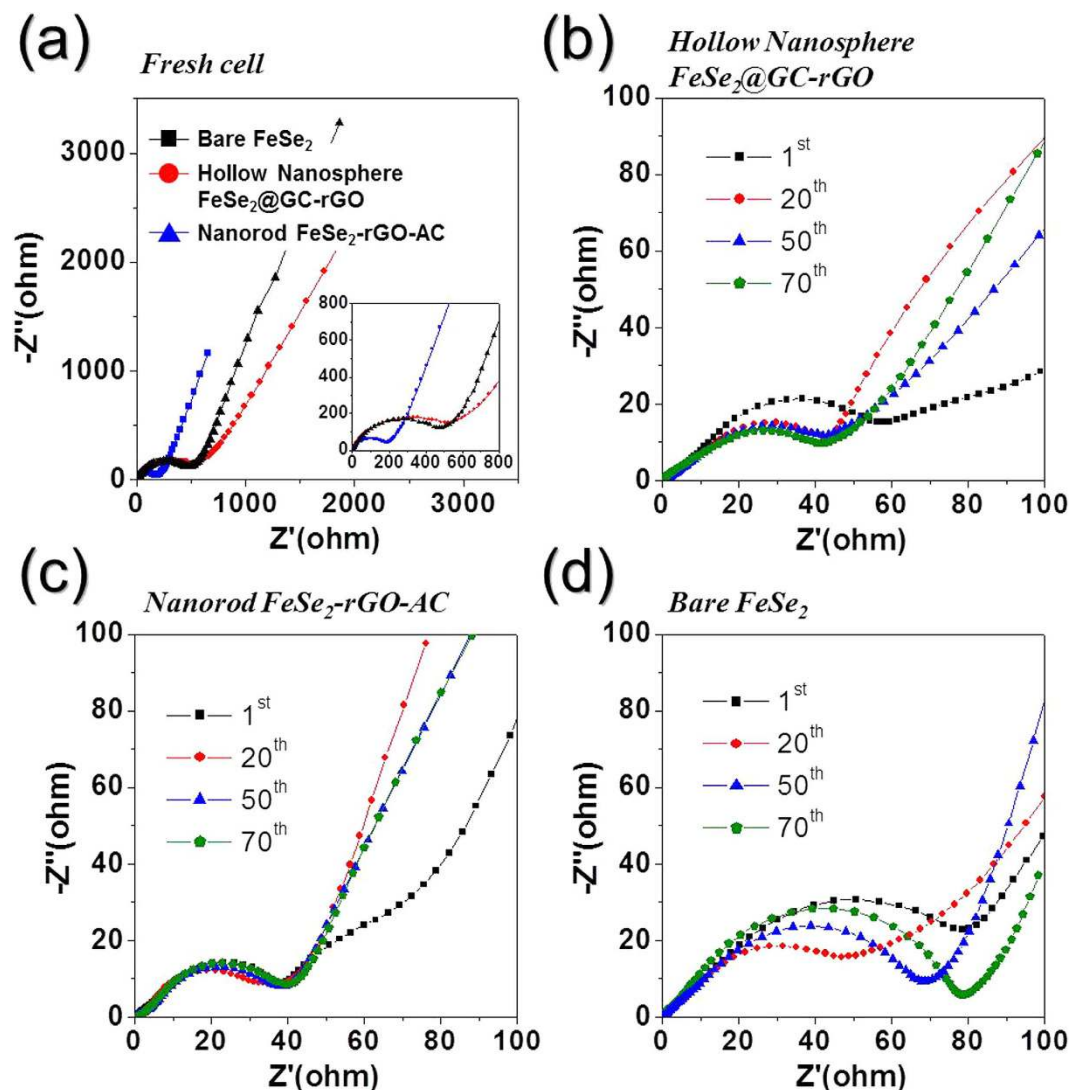


**Figure 6.** Nyquist plots of the hollow nanosphere  $\text{FeSe}_2@GC-rGO$  hybrid, nanorod  $\text{FeSe}_2-rGO-AC$  hybrid, and bare  $\text{FeSe}_2$  nanofibers: (a) before cycling, (b) after cycling of the hollow nanosphere  $\text{FeSe}_2@GC-rGO$  hybrid nanofibers, (c) after cycling of the nanorod  $\text{FeSe}_2-rGO-AC$  hybrid nanofibers, and (d) after cycling of the bare  $\text{FeSe}_2$  nanofibers.

transport pathways for electrons before electrons are transferred to secondary pathway of rGO nano-network matrix, as shown in Fig. 8b. It hence enabled permanent maintenance of good electrical contact with  $\text{FeSe}_2$  hollow spheres. Third,  $\text{FeSe}_2$  hollow spheres were encapsulated inside GC coating layer, which could effectively stabilize the surface of  $\text{FeSe}_2$  hollow sphere, thus leading to the construction of a stable solid electrolyte interphase (SEI) on it and keeping the structural integrity by additionally accommodating the huge volume expansion by  $\text{Na}^+$  diffusion, as shown in Fig. 8c. Simultaneously, GC coating layer inhibited the aggregation of  $\text{FeSe}_2$  nanospheres during repeated charge and discharge processes and thus maintaining the structural and electrical integrity of the structure. As a result, unique structure of the hollow nanosphere  $\text{FeSe}_2@GC-rGO$  hybrid nanofibers combined the aforementioned effects of improved structural stability and maintenance of efficient electron transport pathways during long-term cycling, showing superior electrochemical performances in SIBs.

## Conclusions

We proposed the synthesis of a newly designed nanostructured material comprising graphitic carbon-coated hollow metal chalcogenide nanospheres decorated within rGO nanofibers. The hollow nanosphere  $\text{FeSe}_2@GC-rGO$  hybrid nanofibers selected as the first target material were prepared by applying the nanoscale Kirkendall diffusion process to a conventional electrospinning process. The hollow nanosphere  $\text{FeSe}_2@GC-rGO$  hybrid nanofibers showed superior sodium ion storage properties compared to those of the bare  $\text{FeSe}_2$  and nanorod  $\text{FeSe}_2-rGO-AC$  hybrid nanofibers. The synergetic effects of the highly conductive GC-coated  $\text{FeSe}_2$  hollow nanospheres with high structural stability and fast and continuous transport pathways for electrons during cycling and a highly conductive rGO nano-network matrix resulted in the superior cycling and rate performances of the

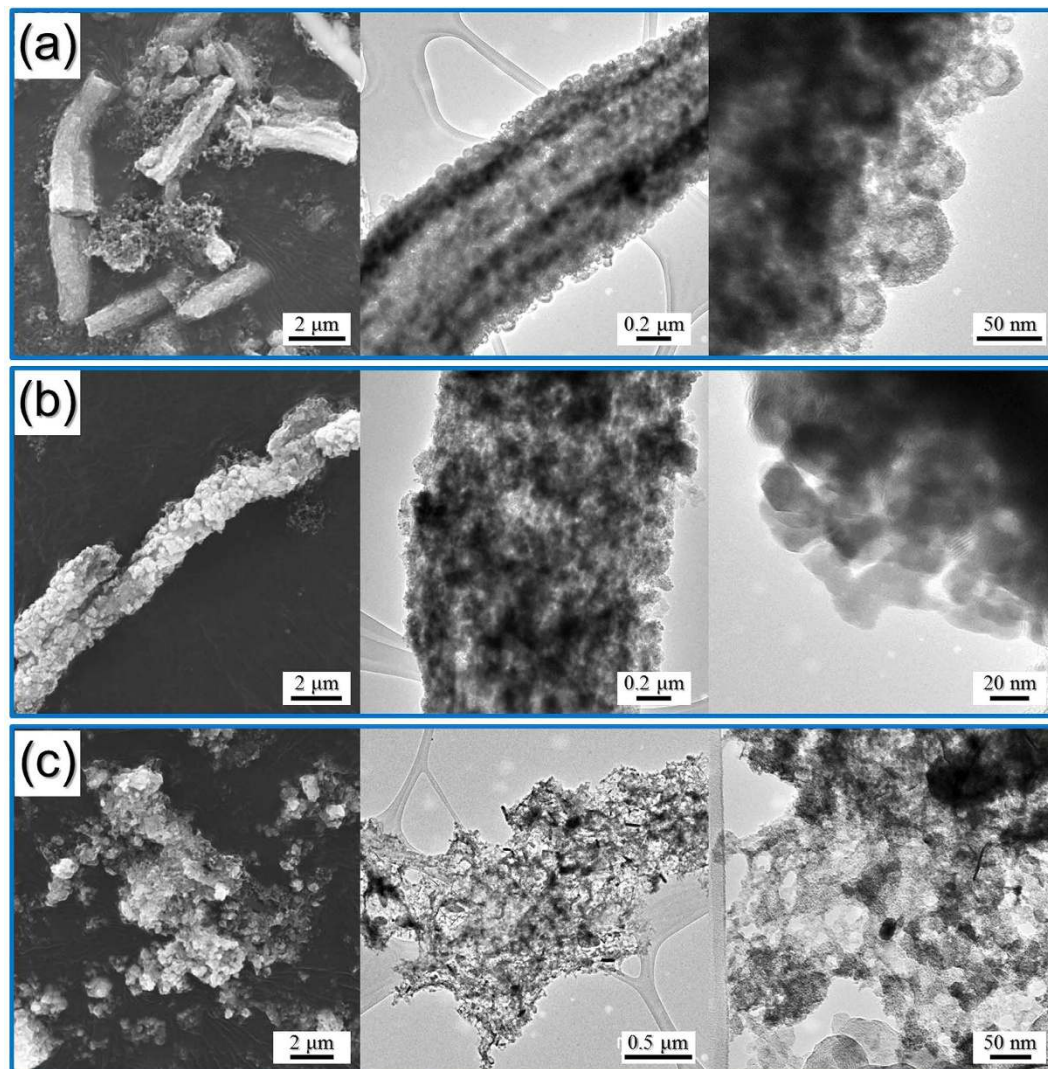


**Figure 7.** Morphologies of the (a) hollow nanosphere  $\text{FeSe}_2$ @GC-rGO hybrid nanofibers, (b) nanorod  $\text{FeSe}_2$ -rGO-AC hybrid nanofibers, and (c) bare  $\text{FeSe}_2$  nanofibers obtained after the 100th cycle.

hollow nanosphere  $\text{FeSe}_2$ @GC-rGO hybrid nanofibers. This simple synthesis method could be widely applied in the preparation of highly conductive GC-coated hollow metal chalcogenide nanospheres decorated within rGO nanofibers for a wide range of applications, including energy storage.

## Materials and Methods

**Sample preparation.** Hollow  $\text{FeSe}_2$ @GC-rGO hybrid nanofibers were prepared via a three-step process. For this preparation,  $\text{Fe}(\text{acac})_3$ -polystyrene (PS)-polyacrylonitrile (PAN) with graphene oxide (GO) [ $\text{Fe}(\text{acac})_3$ -PAN-PS-GO] composite nanofibers were prepared as precursor fibers via an electrospinning process. GO was synthesized from graphite flakes using a modified Hummers method, as described in our previous report<sup>40,41</sup> and then it was freeze-dried. The precursor solution for the electrospinning process was prepared by dissolving 5.0 g of  $\text{Fe}(\text{acac})_3$  (STREM Chemicals, 99%), 1.0 g of PAN (Aldrich,  $M_w$ : 150,000), 2.0 g of PS (Aldrich,  $M_w$ : ~192,000), and 0.2 g of GO in a solution of 30 mL of N,N-dimethylformamide (DMF, Aldrich, 99%) with vigorous stirring overnight. The prepared solution was loaded at a flow rate of 2 mL  $\text{h}^{-1}$  into a plastic syringe equipped with a 25-gauge stainless steel nozzle. The solution was subsequently ejected and electrospun onto a drum collector covered with aluminum foil. During the electrospinning process, the distance between the tip and the collector was maintained at 20 cm, and the rotation of the drum was maintained at 100 rpm. The applied voltage between the collector and the syringe tip was 25 kV. The resultant  $\text{Fe}(\text{acac})_3$ -PAN-PS-GO composite nanofibers were stabilized at 120 °C in air for 1 h. For the  $\text{FeSe}_2$ @GC-rGO hybrid nanofibers, the reduction process was conducted at 500 °C for 3 h in the presence of a gas mixture of 10%  $\text{H}_2$ /Ar; this method produced metallic  $\text{Fe}$ @GC-rGO hybrid nanofibers. The subsequent selenization process was carried out at 300 °C for 6 h in  $\text{H}_2\text{Se}$  gas, formed from commercial selenium-metal powders by hydrogen gas, to produce the hollow  $\text{FeSe}_2$ @GC-rGO hybrid nanofibers. For the selenization process, the metallic  $\text{Fe}$ @GC-rGO hybrid nanofibers and selenium-metal powders were loaded in a covered alumina boat and placed in a quartz-tube reactor. For the  $\text{FeSe}_2$ -rGO-AC (amorphous

## (a) Efficient Conductive Channels of rGO Network Matrix for Electrons

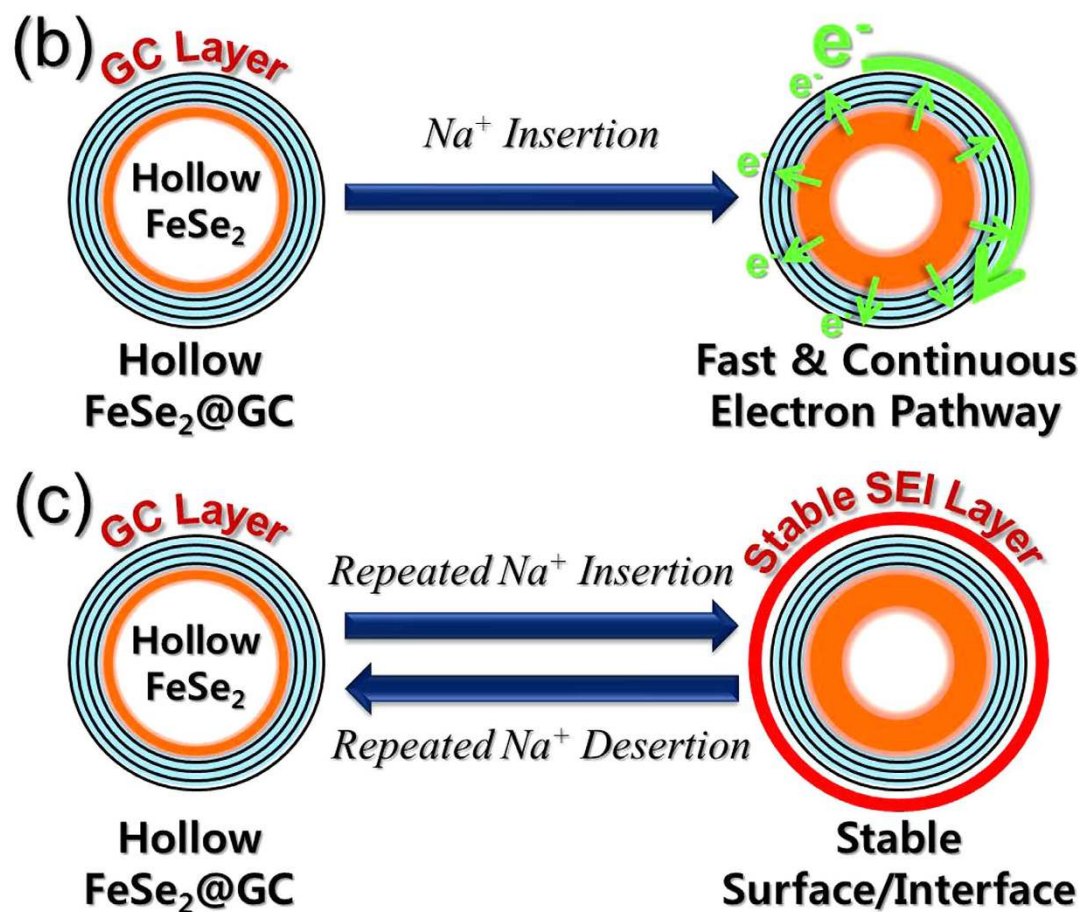
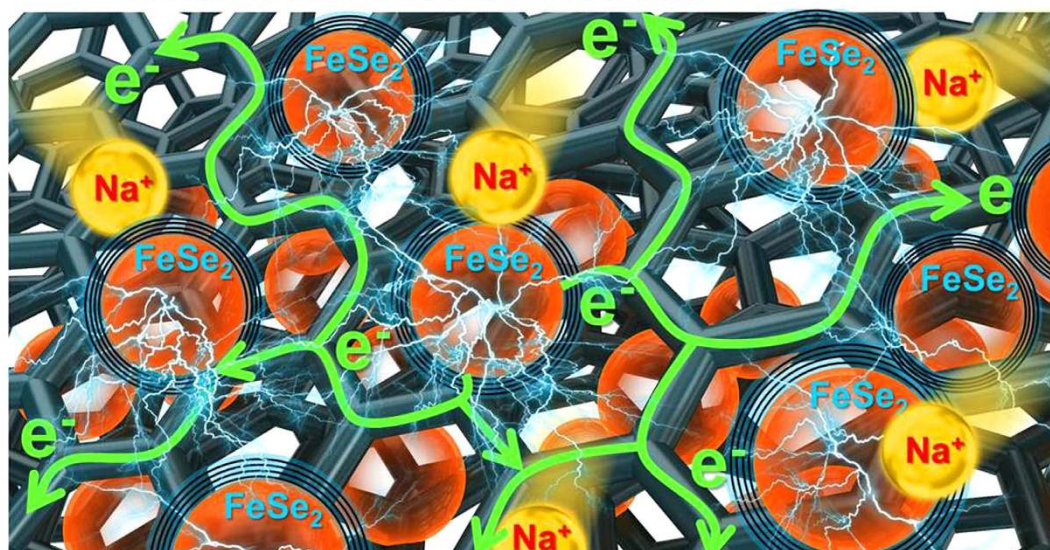


**Figure 8.** (a) 3-D interconnected rGO nano-networks of hollow nanosphere FeSe<sub>2</sub>@GC-rGO hybrid nanofibers with efficient transport pathways for electrons and Na<sup>+</sup> diffusion, (b) illustration of electron transport pathways of GC coating layer covering the hollow FeSe<sub>2</sub>@GC nanosphere upon Na<sup>+</sup> insertion, and (c) the formation of the stable SEI layer on the hollow FeSe<sub>2</sub>@GC nanosphere during cycling.

carbon) hybrid nanofibers comprising FeSe<sub>2</sub> nanorods used for comparison purposes, as-spun Fe(acac)<sub>3</sub>-PAN-PS-GO composite nanofibers were post-treated at 500 °C for 3 h under an Ar atmosphere and subsequently at 300 °C for 6 h in H<sub>2</sub>Se gas for the selenization of the FeO<sub>x</sub> into FeSe<sub>2</sub>. Bare FeSe<sub>2</sub> nanofibers without carbon material were also prepared as another comparison sample. Fe(acac)<sub>3</sub>-PAN-PS composite nanofibers were prepared via electrospinning with identical conditions, as described above, but without containing GO in the precursor solution. The resultant Fe(acac)<sub>3</sub>-PAN-PS composite nanofibers were post-treated at 500 °C for 3 h under an air atmosphere and subsequently at 300 °C for 6 h in H<sub>2</sub>Se gas for their selenization. For simplicity, the FeSe<sub>2</sub>-rG-GC hybrid nanofibers comprising FeSe<sub>2</sub> hollow nanospheres, FeSe<sub>2</sub>-rGO-AC (amorphous carbon) hybrid nanofibers comprising FeSe<sub>2</sub> nanorods, and bare FeSe<sub>2</sub> nanofibers are referred to as “hollow nanosphere FeSe<sub>2</sub>@GC-rGO”, “nanorod FeSe<sub>2</sub>-rGO-AC”, and “bare FeSe<sub>2</sub>”, respectively.

**Characterization techniques.** The microstructures of the nanofibers were observed using field-emission scanning electron microscopy (FESEM, S-4800, Hitachi) and field-emission transmission electron microscopy (TEM, JEM-2100F, JEOL). In addition, their crystal structures were evaluated through X-ray diffraction (XRD, X'Pert PRO MPD) using Cu K<sub>α</sub> radiation ( $\lambda = 1.5418 \text{ \AA}$ ) at the Korea Basic Science Institute (Daegu). X-ray photoelectron spectroscopy (XPS, Thermo Scientific K-Alpha), with a focused monochromatic Al K<sub>α</sub> at 12 kV and 20 mA, was used to analyze the compositions of the specimens. The surface areas of the nanofibers were determined using the Brunauer-Emmett-Teller (BET) method, where N<sub>2</sub> was the adsorbate gas. The structural characterization of the carbon in the specimens was performed via Raman spectra (excited by a 632.8 nm He-Ne laser, Jobin Yvon LabRam HR800) at room temperature. Finally, thermogravimetric analysis (TGA) was performed using a Pyris 1 TGA (Perkin Elmer, temperature range = 25–650 °C, heating rate = 10 °C min<sup>-1</sup>, static air atmosphere).

**Electrochemical measurements.** The electrochemical properties of the fabricated FeSe<sub>2</sub> nanofibers were analyzed by constructing 2032-type coin cells. Each anode was prepared by mixing the active material, carbon black, and sodium carboxymethyl cellulose (CMC) in a weight ratio of 7:2:1. Na metal and microporous polypropylene film were used as the counter electrode and the separator, respectively. The electrolyte was 1 M NaClO<sub>4</sub> (Aldrich) dissolved in a mixture of ethylene carbonate and dimethyl carbonate (EC/DMC, 1:1 v/v), to which 5 wt% fluoroethylene carbonate (FEC) was added. The discharge-charge characteristics of the samples were investigated by cycling the cells in a 0.001–3 V potential range at various current densities. Cyclic voltammograms (CV) were measured at a scan rate of 0.07 mV s<sup>-1</sup>. The dimensions of the anode were 1 cm × 1 cm, and the mass loading was approximately 1.2 mg cm<sup>-2</sup>. The electrochemical impedance was measured using electrochemical-impedance spectroscopy (EIS) over a frequency range of 0.01 Hz to 100 kHz by using the cell taken after fully charged up to 3.0 V.

## References

- Gogotsi, Y. What nano can do for energy storage. *ACS Nano* **8**, 5369–5371 (2014).
- Dubal, D., Ayyad, O., Ruiz, V. & Gómez-Romero, P. Hybrid energy storage: the merging of battery and supercapacitor chemistries. *Chem. Soc. Rev.* **44**, 1777–1790 (2015).
- Wang, J. & Sun, X. Olivine LiFePO<sub>4</sub>: the remaining challenges for future energy storage. *Energy Environ. Sci.* **8**, 1110–1138 (2015).
- Zhang, C., Lv, W., Tao, Y. & Yang, Q.-H. Towards superior volumetric performance: design and preparation of novel carbon materials for energy storage. *Energy Environ. Sci.* **8**, 1390–1403 (2015).
- Goodenough, J. B. & Park, K.-S. The Li-ion rechargeable battery: a perspective. *J. Am. Chem. Soc.* **135**, 1167–1176 (2013).
- Liu, N. *et al.* A yolk-shell design for stabilized and scalable Li-ion battery alloy anodes. *Nano Lett.* **12**, 3315–3321 (2012).
- Reddy, M., Subba Rao, G. & Chowdari, B. Metal oxides and oxysalts as anode materials for Li ion batteries. *Chem. Rev.* **113**, 5364–5457 (2013).
- Kim, S. W., Seo, D. H., Ma, X., Ceder, G. & Kang, K. Electrode materials for rechargeable sodium-ion batteries: potential alternatives to current lithium-ion batteries. *Adv. Energy Mater.* **2**, 710–721 (2012).
- Palomares, V. *et al.* Na-ion batteries, recent advances and present challenges to become low cost energy storage systems. *Energy Environ. Sci.* **5**, 5884–5901 (2012).
- Park, G. D., Cho, J. S. & Kang, Y. C. Novel cobalt oxide-nanobubble-decorated reduced graphene oxide sphere with superior electrochemical properties prepared by nanoscale Kirkendall diffusion process. *Nano Energy* **17**, 17–26 (2015).
- You, Y., Wu, X. L., Yin, Y. X. & Guo, Y. G. High-quality prussian blue crystals as superior cathode materials for room-temperature sodium-ion batteries. *Energy Environ. Sci.* **7**, 1643–1647 (2014).
- Slater, M. D., Kim, D., Lee, E. & Johnson, C. S. Sodium-ion batteries. *Adv. Funct. Mater.* **23**, 947–958 (2013).
- Er, D., Li, J., Naguib, M., Gogotsi, Y. & Shenoy, V. B. Ti<sub>3</sub>C<sub>2</sub> MXene as a high capacity electrode material for metal (Li, Na, K, Ca) ion batteries. *ACS Appl. Mater. Interfaces* **6**, 11173–11179 (2014).
- Cho, J. S., Hong, Y. J. & Kang, Y. C. Design and synthesis of bubble-nanorod-structured Fe<sub>2</sub>O<sub>3</sub>-carbon nanofibers as advanced anode material for Li-ion batteries. *ACS Nano* **9**, 4026–4035 (2015).
- Le Xie, J., Guo, C. X. & Li, C. M. Construction of one-dimensional nanostructures on graphene for efficient energy conversion and storage. *Energy Environ. Sci.* **7**, 2559–2579 (2014).
- Tian, J., Zhao, Z., Kumar, A., Boughton, R. I. & Liu, H. Recent progress in design, synthesis, and applications of one-dimensional TiO<sub>2</sub> nanostructured surface heterostructures: a review. *Chem. Soc. Rev.* **43**, 6920–6937 (2014).
- Wu, L. *et al.* Sb-C nanofibers with long cycle life as an anode material for high-performance sodium-ion batteries. *Energy Environ. Sci.* **7**, 323–328 (2014).
- Cao, Y. *et al.* Sodium ion insertion in hollow carbon nanowires for battery applications. *Nano Lett.* **12**, 3783–3787 (2012).
- Cho, J. S., Hong, Y. J., Lee, J.-H. & Kang, Y. C. Design and synthesis of micron-sized spherical aggregates composed of hollow Fe<sub>2</sub>O<sub>3</sub> nanospheres for use in lithium-ion batteries. *Nanoscale* **7**, 8361–8367 (2015).
- Cho, J. S. & Kang, Y. C. Nanofibers comprising yolk-shell Sn@void/SnO/SnO<sub>2</sub> and hollow SnO/SnO<sub>2</sub> and SnO<sub>2</sub> nanospheres via the Kirkendall diffusion effect and their electrochemical properties. *Small* **11**, 4673–4681 (2015).
- Choi, S. H., Ko, Y. N., Lee, J. K. & Kang, Y. C. 3D MoS<sub>2</sub>-graphene microspheres consisting of multiple nanospheres with superior sodium ion storage properties. *Adv. Funct. Mater.* **25**, 1780–1788 (2015).
- Shen, L. *et al.* Formation of nickel cobalt sulfide ball-in-ball hollow spheres with enhanced electrochemical pseudocapacitive properties. *Nat. Commun.* **6** (2015).

23. Cho, J. S., Hong, Y. J. & Kang, Y. C. Electrochemical properties of fiber-in-tube and filled-structured TiO<sub>2</sub> nanofiber anode materials for lithium-ion batteries. *Chem. -Eur. J.* **21**, 11082–11087 (2015).
24. Hong, Y. J., Son, M. Y. & Kang, Y. C. One-pot facile synthesis of double-shelled SnO<sub>2</sub> yolk-shell-structured powders by continuous process as anode materials for Li-ion batteries. *Adv. Mater.* **25**, 2279–2283 (2013).
25. Jiang, H. *et al.* Rational design of MnO/carbon nanopeapods with internal void space for high-rate and long-life Li-ion batteries. *ACS Nano* **8**, 6038–6046 (2014).
26. Wu, X. L., Guo, Y. G. & Wan, L. J. Rational design of anode materials based on group IVA elements (Si, Ge, and Sn) for lithium-ion batteries. *Chem. -Asian J.* **8**, 1948–1958 (2013).
27. Chen, K., Song, S., Liu, F. & Xue, D. Structural design of graphene for use in electrochemical energy storage devices. *Chem. Soc. Rev.* **44**, 6230–6257 (2015).
28. Raccichini, R., Varzi, A., Passerini, S. & Scrosati, B. The role of graphene for electrochemical energy storage. *Nat. Mater.* **14**, 271–279 (2015).
29. Yu, M. *et al.* Building three-dimensional graphene frameworks for energy storage and catalysis. *Adv. Funct. Mater.* **25**, 324–330 (2015).
30. Anasori, B., Beidaghi, M. & Gogotsi, Y. Graphene–transition metal oxide hybrid materials. *Mater. Today* **17**, 253–254 (2014).
31. Ferrari, A. *et al.* Raman spectrum of graphene and graphene layers. *Phys. Rev. Lett.* **97**, 187401 (2006).
32. Huang, S. *et al.* 3D hierarchical FeSe<sub>2</sub> microspheres: controlled synthesis and applications in dye-sensitized solar cells. *Nano Energy* **15**, 205–215 (2015).
33. Zhang, K., Hu, Z., Liu, X., Tao, Z. & Chen, J. FeSe<sub>2</sub> microspheres as a high-performance anode material for Na-ion batteries. *Adv. Mater.* **27**, 3305–3309 (2015).
34. Kim, Y. *et al.* SnSe alloy as a promising anode material for Na-ion batteries. *Chem. Commun.* **51**, 50–53 (2015).
35. Ni, S., Yang, X. & Li, T. Fabrication of a porous NiS/Ni nanostructured electrode via a dry thermal sulfuration method and its application in a lithium ion battery. *J. Mater. Chem.* **22**, 2395–2397 (2012).
36. Yan, X. *et al.* Synthesis of hollow nickel oxide nanotubes by electrospinning with structurally enhanced lithium storage properties. *Mater. Lett.* **136**, 74–77 (2014).
37. Kim, J. H. & Kang, Y. C. Electrochemical properties of micron-sized, spherical, meso- and macro-porous Co<sub>3</sub>O<sub>4</sub> and CoO–carbon composite powders prepared by a two-step spray drying process. *Nanoscale* **6**, 4789–4795 (2014).
38. Sun, Y., Hu, X., Luo, W., Xia, F. & Huang, Y. Reconstruction of conformal nanoscale MnO on graphene as a high-capacity and long-life anode material for lithium ion batteries. *Adv. Funct. Mater.* **23**, 2436–2444 (2013).
39. Cho, J. S., Won, J. M., Lee, J.-H. & Kang, Y. C. Synthesis and electrochemical properties of spherical and hollow-structured NiO aggregates created by combining the Kirkendall effect and Ostwald ripening. *Nanoscale* **7**, 19620–19626 (2015).
40. Park, G. D., Cho, J. S. & Kang, Y. C. Sodium-ion storage properties of nickel sulfide hollow nanospheres/reduced graphene oxide composite powders prepared by a spray drying process and the nanoscale Kirkendall effect. *Nanoscale* **7**, 16781–16788 (2015).
41. Park, G. D., Cho, J. S. & Kang, Y. C. Multiphase and double-layer NiFe<sub>2</sub>O<sub>4</sub>@NiO-hollow-nanosphere-decorated reduced graphene oxide composite powders prepared by spray pyrolysis applying nanoscale Kirkendall diffusion *ACS Appl. Mater. Interfaces* **7**, 16842–16849 (2015).

## Acknowledgements

This research was supported by a grant from the Intelligent Synthetic Biology Center of Global Frontier Project (2011-0031955) funded by the Ministry of Science, ICT and Future Planning, Republic of Korea. This work was supported by a National Research Foundation of Korea (NRF) grant funded by the Korea government (MEST) (NRF-2015R1A2A1A15056049).

## Author Contributions

J.S.C., J.K.L. and Y.C.K. devised the concept, designed the experiment, and wrote the manuscript. J.S.C. performed the experiments and analyzed the data. Y.C.K. and J.K.L. supervised the project. All authors discussed the results and contributed in this manuscript.

## Additional Information

**Supplementary information** accompanies this paper at <http://www.nature.com/srep>

**Competing financial interests:** The authors declare no competing financial interests.

**How to cite this article:** Cho, J. S. *et al.* Graphitic Carbon-Coated FeSe<sub>2</sub> Hollow Nanosphere-Decorated Reduced Graphene Oxide Hybrid Nanofibers as an Efficient Anode Material for Sodium Ion Batteries. *Sci. Rep.* **6**, 23699; doi: 10.1038/srep23699 (2016).



This work is licensed under a Creative Commons Attribution 4.0 International License. The images or other third party material in this article are included in the article's Creative Commons license, unless indicated otherwise in the credit line; if the material is not included under the Creative Commons license, users will need to obtain permission from the license holder to reproduce the material. To view a copy of this license, visit <http://creativecommons.org/licenses/by/4.0/>